

X-Ray and Gamma-Ray Emission from the PSR 1259-63/Be Star System

Kenji MURATA, Hidenori TAMAKI, Hideki MAKI, and Noriaki SHIBAZAKI
Department of Physics, Rikkyo University, Nishi-Ikebukuro, Tokyo 171-8501, Japan
maki@hel.rikkyo.ne.jp

(Received 2002 September 2; accepted 2003 January 31)

Abstract

PSR 1259-63 is a radio pulsar orbiting a Be star in a highly eccentric orbit. Soft and hard X-rays are observed from this binary system. We apply the shock powered emission model to this system. The collision of the pulsar and Be star winds forms a shock, which accelerates electrons and positrons to the relativistic energies. We derive the energy distribution of relativistic electrons and positrons as a function of the distance from the shock in the pulsar nebula. We calculate the X-rays and γ -rays emitted from the relativistic electrons and positrons in the nebula at various orbital phases, taking into account the Klein-Nishina effect fully. The shock powered emission model can explain the observed X-ray properties approximately. We obtain from the comparison with observations that a fraction of ~ 0.1 of the pulsar spin-down luminosity should be transformed into the relativistic electrons and positrons. We find that the magnetization parameter of the pulsar wind, the ratio of the Poynting flux to the kinetic energy flux, is ~ 0.1 immediately upstream of the termination shock of the pulsar wind, and may decrease with distance from the pulsar. We predict the flux of 10 MeV–100 GeV γ -rays which may be nearly equal to the detection threshold in the future projects.

Key words: Pulsars — Stars: Be — Stars: individual (PSR B1259-63) — Stars: individual (SS2883) — X-rays: binaries

1. Introduction

PSR 1259-63 is a 48 ms radio pulsar orbiting a Be star in a 3.4 yr orbit with eccentricity of 0.86 (Johnston et al. 1992a; Manchester et al. 1995). The binary companion is a 10th magnitude B2e star SS 2883, whose mass and radius are estimated to be $\sim 10 M_{\odot}$ and $\sim 6-10 R_{\odot}$, respectively (Johnston et al. 1992b). The distance may be ~ 2 kpc (Taylor & Cordes 1993; Johnston et al. 1994).

The PSR 1259-63/SS 2883 system has been observed in the X-ray and γ -ray bands ranging from 1 keV to ~ 1 TeV (Cominsky, Roberts & Johnston 1994; Greiner, Tavani & Belloni 1995; Kaspi et al. 1995; Grove et al. 1995; Tavani et al. 1996; Hirayama et al. 1996; Hirayama et al. 1999; Kawachi et al. 2002). The X-ray spectra are well represented by a power law function. The X-ray luminosity in the 1–10 keV band is $\sim 10^{33} - 10^{34}$ erg \cdot s $^{-1}$. The spectral slope and luminosity of X-rays vary with orbital phase. The pulsation is absent in the X-ray intensity. Only upper limits are reported for the high energy γ -ray emission above 1 MeV including TeV γ -rays (Tavani et al. 1996; Kawachi et al. 2002).

Tavani, Arons & Kaspi (1994) and Tavani & Arons (1997) developed the shock powered emission model after they examined a few possibilities for the high energy emission from the PSR 1259-63/SS 2883 system. The pulsar wind collides with the stellar wind ejected from the Be star, forming a shock. The shock accelerates the pulsar wind particles, electrons and positrons, to the relativistic high energies (Hoshino et al. 1992; Hoshino & Shimada 2002). The relativistic electrons and positrons in the nebula radiate keV–MeV photons through the synchrotron emission and GeV–TeV photons through the inverse Compton scattering of the photons from the Be star. Model calculations for the X-ray spectral and luminosity variation with orbital phase reproduced observations. Note, however, that the approximation they adopted for the Klein-Nishina effect is not appropriate especially to see the spectral properties. Some conclusions in Tavani & Arons (1997) may be modified if we include the Klein-Nishina effect correctly in calculations (Kirk, Ball & Skjaeraasen 1999).

Kirk, Ball & Skjaeraasen (1999) calculated light curves for the hard γ -ray emission at energies up to several TeV, including the Klein-Nishina effect and adopting several approximations for the inverse Compton scattering process. They use the continuous approximation for the electron energy loss and the delta function approximation for the distribution of target and scattered photons. They find the light curve of hard γ -rays especially at 100 GeV becomes asymmetric with respect to periastron since the inverse Compton emissivity depends on the scattering angle (the angle between the line of sight and the vector connecting the stars). They also show that we can expect the significantly larger flux of hard γ -rays when the inverse Compton cooling dominates over the synchrotron cooling. We should note that the upper limit on the \sim TeV γ -ray flux, recently set by the CANGAROO collaboration, is almost equal to the flux they predict.

We study the shock powered emission model for the PSR 1259-63/Be Star System. We calculate the X-rays and γ -rays emitted from the shock accelerated electrons and positrons at various orbital phases, taking into account the Klein-Nishina effect and the distributions for the target and scattered photons.

This paper is organized as follows. We describe a pulsar wind and a termination shock briefly in section 2. We estimate cooling times of relativistic electrons and positrons injected into the downstream region of the shock in section 3. We follow the evolution of particle

distribution in the shock downstream region and calculate the X-rays and γ -rays emitted from the nebula at various orbital phases in section 4. Comparing with X-ray observations, we set constraints on the property of a pulsar wind in section 5. In the last section we give a few concluding remarks.

2. A Pulsar Wind and a Shock

Pulsars lose a large fraction of their rotational energy in the form of relativistic MHD winds. The pulsar wind carries e^+e^- pairs, possibly together with a small admixture of ions (Hoshino et al. 1992) and also conveys electromagnetic energy. The energy flux of the pulsar wind at the distance r from the pulsar can be expressed as

$$F_w = \frac{\dot{E}_{\text{rot}}}{\Omega_w r^2}, \quad (1)$$

where \dot{E}_{rot} is the spin-down luminosity of the pulsar and Ω_w the solid angle of the wind. We introduce the magnetization parameter σ , defined by the ratio of the Poynting flux to the kinetic energy flux,

$$\sigma = \frac{B_1^2}{4\pi\gamma_w\rho c^2}, \quad (2)$$

where γ_w and ρ are respectively the Lorentz factor and mass density of the pulsar wind, B_1 is the magnetic field, and c is the speed of light. Then, the energy flux can also be written as

$$F_w = \gamma_w\rho c^2(1 + \sigma)c. \quad (3)$$

Combining equations (1), (2) and (3), we have

$$B_1 = \left(\frac{\sigma}{1 + \sigma}\right)^{1/2} \left(\frac{4\pi}{\Omega_w}\right)^{1/2} \left(\frac{\dot{E}_{\text{rot}}}{c}\right)^{1/2} \frac{1}{r}. \quad (4)$$

The strength of magnetic field decreases in inverse proportion to the distance from the pulsar.

The pulsar wind collides with the stellar wind ejected from the Be star, forming a shock. We estimate the shock location from the balance in dynamical pressure between the pulsar and stellar winds,

$$\frac{\dot{E}_{\text{rot}}}{\Omega_w r^2 c} = \frac{\dot{M}_B v_B}{\Omega_B (a - r)^2}, \quad (5)$$

where v_B , Ω_B , and \dot{M}_B are respectively the velocity, solid angle and rate of the mass outflow from the Be star and a is the orbital separation of the binary system (see Melatos, Johnston & Melrose 1995 for the more actual shape of the shock). Then, the shock distance r_s is

$$r_s = \xi \cdot a \quad (6)$$

where ξ is given by

$$\xi^{-1} = \sqrt{\frac{\Omega_w}{\Omega_B} \cdot \frac{\dot{M}_B v_B c}{\dot{E}_{\text{rot}}}} + 1. \quad (7)$$

If the pulsar and stellar winds are spherically symmetric, ξ remains constant throughout the orbit, no matter how eccentric it is. In the PSR B1259-63/SS 2883 system the orbital separation and hence the shock distance may vary by an order of magnitude between periastron and apastron because of the deformed binary orbit with eccentricity of $e = 0.86$. Note that the shock distance depends also on the physical parameters and geometry of pulsar and Be star winds, which are not so certain. Hence, in the following we treat ξ as a free parameter which can be determined from the comparison with observations.

The shock in the pulsar wind compresses the magnetic field as well as the wind matter. The field strength B_2 at the downstream side of the shock is calculated from equation (4) together with the relativistic MHD shock conditions (Kennel & Coroniti 1984),

$$B_2(r_s) = 3B_1(r_s). \quad (8)$$

The shock accelerates the pulsar wind particles, electrons and positrons, to the relativistic high energies (Hoshino et al. 1992). We assume that the acceleration time is short compared to the radiative cooling times and the flow time of the shock downstream region. We adopt the power law distribution for the accelerated electrons and positrons in the range of $\gamma_1 < \gamma < \gamma_2$

$$N_0(\gamma) = K\gamma^{-p}, \quad (9)$$

where $N_0(\gamma)$ is the density of relativistic electrons and positrons injected at the shock, γ the Lorentz factor, p the power law index and K the constant. We assume that the distributions of accelerated particles at the shock are the same and given by equation (9) irrespective of the binary phase. A fraction ε_a of the pulsar spin-down luminosity is transformed into the relativistic electrons and positrons. The constant K in equation (9) is then given by

$$K = (p - 2)\gamma_1^{p-1} \frac{\varepsilon_a \dot{E}_{\text{rot}}}{\Omega_w r_s^2 \gamma_1 m c^2 (c/3)} \quad (10)$$

for $p \neq 2$. In equation (10) m is the electron mass. The accelerated relativistic particles are injected into the downstream region at the shock and flow in the downstream region with a speed of $c/3$.

3. Cooling Times

Relativistic electrons and positrons lose energy through the synchrotron and inverse Compton processes, emitting X-rays and γ -rays, as they flow along the stream line in the postshock region. Relativistic electrons and positrons may also suffer from the adiabatic energy loss. Here we estimate the cooling times of the relativistic electrons and positrons using the physical parameters at the shock.

The flow time of the postshock stream is given approximately by

$$\tau_f = \frac{r_s}{c/3}. \quad (11)$$

The flow time τ_f denotes approximately the residence time of relativistic electrons and positrons in the emission nebula. The flow time τ_f also represents the cooling time of the relativistic particles due to the adiabatic energy loss. Note that the power law index of the energy distribution of relativistic electrons and positrons remains unchanged throughout adiabatic cooling.

The typical energy of synchrotron photons is

$$\varepsilon \sim 0.23\hbar \left(\frac{3\gamma^2 e B_2}{2mc} \right), \quad (12)$$

where ε is the photon energy, e the electron charge and \hbar the Planck constant. The synchrotron cooling time is calculated by

$$\tau_s = \frac{3mc}{4\sigma_T U_{B_2} \gamma}, \quad (13)$$

where σ_T is the Thomson cross section and U_{B_2} is the magnetic energy density,

$$U_{B_2}(r_s) = \frac{B_2^2}{8\pi}. \quad (14)$$

The relativistic electrons and positrons lose energy by scattering off the photons emitted from the Be star. The typical energy of the scattered photons is

$$\varepsilon \sim \begin{cases} \gamma^2 \varepsilon_0 & (\gamma \varepsilon_0 \ll mc^2) \\ \gamma mc^2 & (\gamma \varepsilon_0 \gg mc^2) \end{cases}, \quad (15)$$

where ε_0 is the typical energy of photons from the Be star. In the Thomson limit, where $\gamma \varepsilon_0 \ll mc^2$, the inverse Compton cooling time is calculated by

$$\tau_{ic} = \frac{3mc}{4\sigma_T U_p \gamma}, \quad (16)$$

where U_p is the energy density of photons from the Be star. The photon energy density U_p at the shock is estimated by

$$U_p(r_s) = \frac{R_B^2 \sigma_B T^4}{(a - r_s)^2 c}, \quad (17)$$

where R_B is the radius of the Be star, T the effective surface temperature and σ_B the Stefan-Boltzman constant. In the Klein-Nishina limit, where $\gamma \varepsilon_0 \gg mc^2$, the inverse Compton scattering becomes less efficient and furthermore, a large fraction of the electron (positron) energy can be lost in one scattering. Hence, in general, we need to compute the average energy loss rate $\langle -\dot{\gamma}_{ic} \rangle$ using the Klein-Nishina formula, in which case

$$\langle -\dot{\gamma}_{ic} \rangle = \int_1^\gamma P(\gamma, \gamma') (\gamma - \gamma') d\gamma', \quad (18)$$

where $P(\gamma, \gamma') d\gamma' dt$ is the probability that an electron with energy γ will undergo a collision causing it to fall down to the lower energy state between γ' and $\gamma' + d\gamma'$ in time dt . Here we calculate the probability $P(\gamma, \gamma')$ for a blackbody photon field. For details of $P(\gamma, \gamma')$ we refer the readers to Jones (1968) and Blumenthal (1970). Then, the inverse Compton cooling time is redefined by

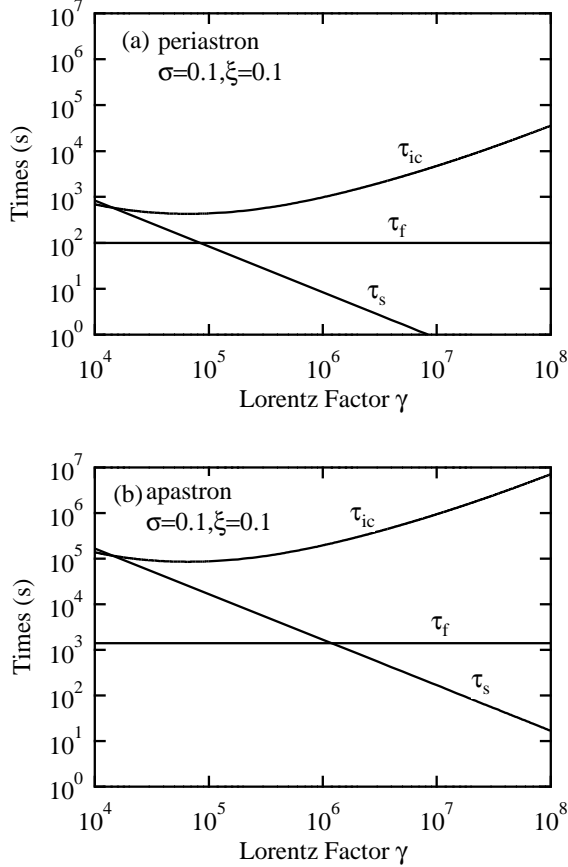


Fig. 1. Cooling and flow times of relativistic electrons and positrons at periastron (a) and apastron (b) plotted against the Lorentz factor. τ_s , τ_{ic} and τ_f express the synchrotron cooling time, the inverse Compton cooling time and the flow time, respectively. The model parameters used are $\sigma = 0.1$ and $\xi = 0.1$. The synchrotron cooling dominates over the inverse Compton cooling. The increase of τ_{ic} for larger γ reflects the Klein-Nishina effect.

$$\tau_{ic} = \frac{\gamma}{\langle -\dot{\gamma}_{ic} \rangle}. \quad (19)$$

Note that equation (19) reduces to equation (16) in the Thomson limit.

We illustrate the cooling times at periastron and apastron as a function of the Lorentz factor of relativistic electrons and positrons in figure 1. The binary separations at periastron and apastron are $a = 9.9 \times 10^{12}$ cm and $a = 1.4 \times 10^{14}$ cm, respectively (Manchester et al. 1995). The spin down luminosity of the pulsar is $\dot{E}_{rot} \sim 8.28 \times 10^{35}$ erg/s. We take the solid angle of the pulsar wind to be $\Omega_w \sim \pi$. We adopt $R_B \sim 11R_\odot$ and $T \sim 2.7 \times 10^4$ K for the radius and effective surface temperature of the Be star (Johnston et al. 1992b). The physical parameters σ and ξ are chosen as $\sigma = 0.1$ and $\xi = 0.1$. The field strengths at the shock are $B_2 \sim 9.6$ G and $B_2 \sim 0.67$ G for periastron (figure 1a) and apastron (figure 1b), respectively. The synchrotron cooling time decreases simply with increasing Lorentz factor. On the other hand, the inverse Compton cooling time first decreases and then increases with increasing Lorentz factor. This behavior

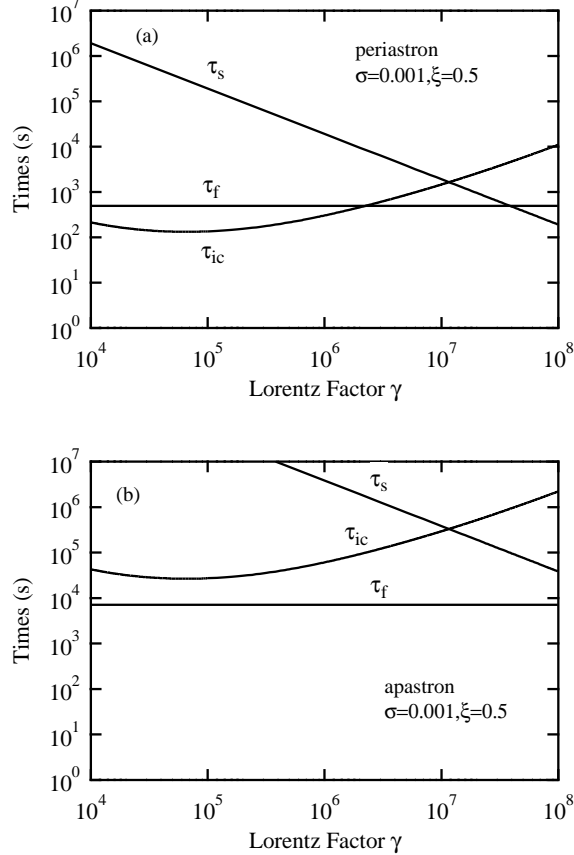


Fig. 2. Cooling and flow times of relativistic electrons and positrons at periastron (a) and apastron (b) for the case with $\sigma = 0.001$ and $\xi = 0.5$. The inverse Compton cooling dominates over the synchrotron cooling.

is a consequence of the Klein-Nishina effect that the inverse Compton scattering becomes less efficient at higher energies. The synchrotron emission dominates over the inverse Compton scattering at both periastron and apastron for $\gamma \gtrsim 10^5$, which approximately corresponds to synchrotron emission in the X-ray band. Both the synchrotron and inverse Compton cooling times are longer at apastron than at periastron since the field strength and photon energy density are lower at apastron. Note that the synchrotron cooling time becomes shorter than the flow time at $\gamma > \gamma_b \sim 10^5$ and at $\gamma > \gamma_b \sim 10^6$ in figure 1a and figure 1b, respectively. As shown in section 4, there appears a break-off in the slope of the particle distribution and emission spectrum at the energy corresponding to γ_b since higher energy particles are lost rapidly.

We depict the cooling times also for the parameters $\sigma = 0.001$ and $\xi = 0.5$ in figure 2. The field strengths at the shock are $B_2 \sim 0.2$ G and $B_2 \sim 0.01$ G for periastron (figure 2a) and apastron (figure 2b), respectively. The magnetic fields adopted are considerably weaker than those in figure 1. The energy densities of photons are higher than those in figure 1 since the shock is located closer to the Be star. The inverse Compton scattering dominates over the

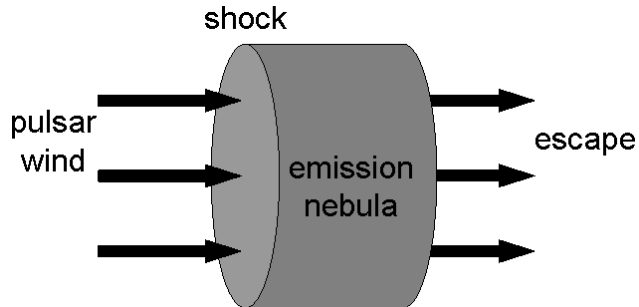


Fig. 3. Schematic diagram of an emission nebula.

synchrotron emission and hence determines the energy distribution of relativistic electrons and positrons in the emission nebula.

4. Nebula Emission

An emission nebula, which radiates X-rays and γ -rays, is formed in the shock downstream region. The geometry of the emission nebula depends on the properties of the pulsar and Be star winds. Here, for simplicity, we approximate the nebula geometry by a cylinder that has the cross section of $\Omega_w r_s^2$ and the length of $L \sim r_s$ (figure 3). The accelerated electrons and positrons are injected at the termination shock (one end of the cylinder) and flow in the direction of the central axis of a cylinder together with the shocked pulsar wind, keeping the density constant. Relativistic electrons and positrons emit X-rays and γ -rays through the synchrotron and inverse Compton processes. At the other end of the cylinder they escape out of the emission nebula.

4.1. Distribution of Relativistic Electrons and Positrons

The energy distribution of relativistic electrons and positrons varies as they flow away from the shock, following a streamline, because of the radiative energy loss. The evolution of the particle distribution $N(\gamma, t)$ can be described by the integro-differential equation,

$$\begin{aligned}
 \frac{\partial N(\gamma, t)}{\partial t} + \frac{\partial}{\partial \gamma} [\dot{\gamma} N(\gamma, t)] \\
 + N(\gamma, t) \int_1^\gamma d\gamma' P(\gamma, \gamma') - \int_\gamma^\infty d\gamma' N(\gamma', t) P(\gamma', \gamma) \\
 = N(\gamma, 0) \delta(t) - \frac{N(\gamma, t)}{\tau_{\text{f}}},
 \end{aligned} \tag{20}$$

where t is the time that elapsed after the injection of relativistic particles at the shock and is related to the distance x from the shock by $x = (c/3)t$. $\dot{\gamma}$ in equation (20) represents the energy loss due to the synchrotron process, while the third and fourth terms in the left-hand side represent the energy loss due to the inverse Compton process. The first term in the right-hand side of equation (20) represents the source of the relativistic electrons and positrons (equation (9)), supplied at $t=0$ (or at the shock), while the second term represents their escape

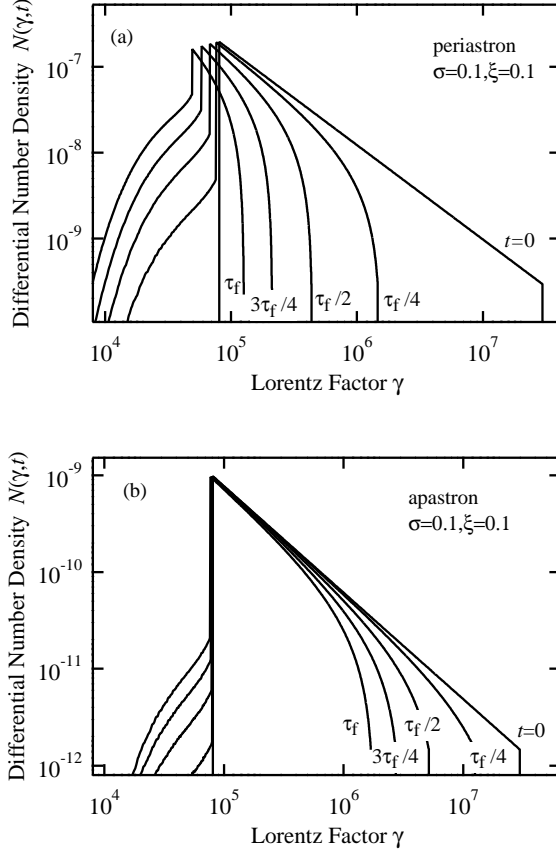


Fig. 4. Variation of the energy distribution of relativistic electrons and positrons with time (or with distance from the shock) at periastron (a) and apastron (b). The parameters for the magnetization and shock position are taken as $\sigma = 0.1$ and $\xi = 0.1$. The power law function, characterized by the index of $p = 2.1$, the minimum Lorentz factor of $\gamma_1 = 8 \times 10^4$, and the maximum Lorentz factor of $\gamma_2 = 3 \times 10^7$, is used as the input particle distribution. The particle distributions at $t = 0$, $\tau_f/4$, $\tau_f/2$, $3\tau_f/4$ and τ_f are illustrated. The particles are lost from higher energies with time due to the radiative loss, especially synchrotron loss, and accumulate at lower energies. The variation of the particle distribution at periastron is much larger than that at apastron because of the efficient synchrotron cooling.

from the emission nebula. The adiabatic energy loss is ignored.

We show in figure 4 how the energy distribution of relativistic electrons and positrons changes with time or with distance from the shock for the periastron and apastron cases. Here the parameters for the magnetization and shock position are taken as $\sigma = 0.1$ and $\xi = 0.1$, while the parameters for the input particle distribution are taken as $p = 2.1$, $\gamma_1 = 8 \times 10^4$, and $\gamma_2 = 3 \times 10^7$. The radiative loss is mainly determined by the synchrotron process. The loss of relativistic electrons and positrons occurs faster at higher Lorentz factors and extends to the lower Lorentz factors as with time. The particles accumulate at $\gamma < \gamma_1$ with time since the particles fall from higher to lower Lorentz factors losing energy. The particle distribution undergoes a large variation with time due to the efficient synchrotron cooling in the periatron

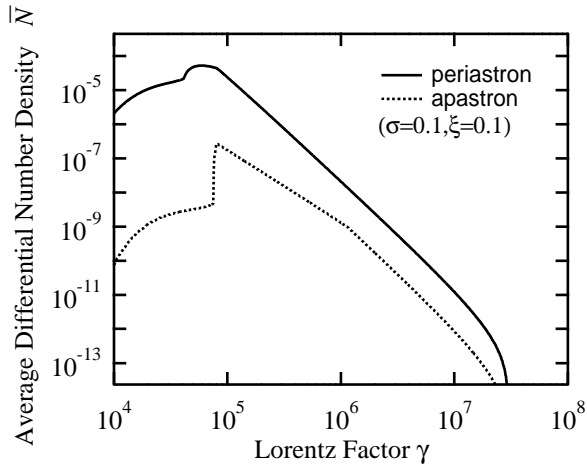


Fig. 5. Average distributions of relativistic electrons and positrons in the nebula at periastron (solid line) and at apastron (dotted line). The model parameters used are the same as those in figure 4. The synchrotron cooling is dominant over the inverse Compton cooling. The slope of the particle distribution steepens by one, compared to the input particle distribution, above $\gamma_b \sim 10^5$ and $\gamma_b \sim 10^6$, where the synchrotron cooling time becomes equal to the flow time (figure 1), respectively for the periastron and apastron cases.

case (figure 4a), whereas in the apastron case (figure 4b) the variation is less significant.

We integrate the relativistic electrons and positrons, shown in figure 4, over an entire emission nebula and then divide the integrated one by the nebula volume. We obtain the average energy distribution for the relativistic electrons and positrons in the nebula, which we show in figure 5. As expected from figure 1, we observe that the slope of the particle distribution steepens by one, compared to the input particle distribution, above $\gamma_b \sim 10^5$ and $\gamma_b \sim 10^6$, where the synchrotron cooling time becomes shorter than the flow time (figure 1), in the periastron and apastron cases, respectively. Note that the total number of relativistic electrons and positrons in the emission nebula is larger at apastron than at periastron, contrary to the particle density, since the volume of the emission nebula is assumed to be in proportion to r_s^3 .

Next, let us consider the average energy distribution of relativistic electrons and positrons when the energy loss of particles is determined mainly by the inverse Compton process. Adopting the same values for parameters σ and ξ as those in figure 2, we plot the average distribution at periastron in figure 6. In the solid line we include both the inverse Compton and synchrotron cooling although the inverse Compton cooling is far dominant over the synchrotron cooling. In the dotted line we retain only the synchrotron cooling, suppressing the inverse Compton cooling completely, in order to understand the effect of the inverse Compton process on the particle distribution. We observe in the solid line the flattening rather than steepening for the slope of the particle distribution at $\gamma > 10^5$, contrary to the synchrotron dominant case in figure 5. This flattening is caused by the Klein-Nishina effect. As seen from figure 2, the inverse Compton cooling is most efficient at $\gamma \sim 10^5$ and then becomes less efficient

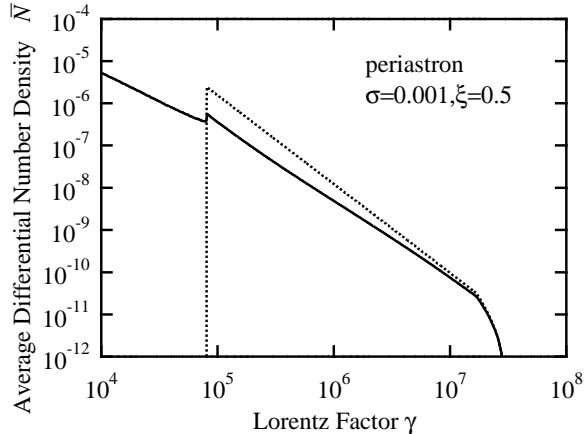


Fig. 6. Average distribution of relativistic electrons and positrons at periastron for the case with $\sigma = 0.001$ and $\xi = 0.5$. The inverse Compton cooling is dominant over the synchrotron cooling. In the solid line both the inverse Compton and synchrotron cooling are included, while in the dotted line the inverse Compton cooling is suppressed completely. The inverse Compton cooling causes flattening in the slope of the particle distribution.

at $\gamma > 10^5$ because of the Klein-Nishina effect. The increase of the cooling time with increasing γ yields the flattening in the particle distribution.

4.2. Radiation Spectrum

The relativistic electrons and positrons in the nebula radiate keV–MeV photons through the synchrotron process and GeV–TeV photons through the inverse Compton process. We calculate the spectrum of X-rays and γ -rays radiated from the whole nebula, taking fully into account the particle distribution, the Klein-Nishina effect, the Planck distribution for the target photons of the inverse Compton scattering and the spectral function for synchrotron emission. We illustrate the X-ray and γ -ray spectra expected at periastron and apastron in figure 7, where we adopt the same particle distribution and physical parameters as those used in figure 5.

The spectral shape in the X-ray band is well represented by a power law function with exponents of ~ 1 and ~ 0.7 at periastron and apastron, respectively. The steeper gradient at periastron is a direct consequence of a steeper particle distribution at periastron, caused by the efficient synchrotron cooling. The X-ray luminosity decreases slightly with the binary separation. This weak dependence on the binary separation of the X-ray luminosity can easily be understood by using equations (4), (6), (8) and (9). Physically, the insensitivity of the X-ray luminosity arises because the injected energy remains constant over the orbit and this is converted almost completely into X-rays. If we adopt the larger values for the maximum Lorentz factor γ_2 , the spectrum of the synchrotron component extends to higher energies. Hence, if the sensitivity of observations in the 10 MeV–1 GeV band is improved in future, the maximum Lorentz factor γ_2 of the particle acceleration would be determined.

The inverse Compton component peaks at a γ -ray energy of $\sim 10^{10}$ eV, as expected

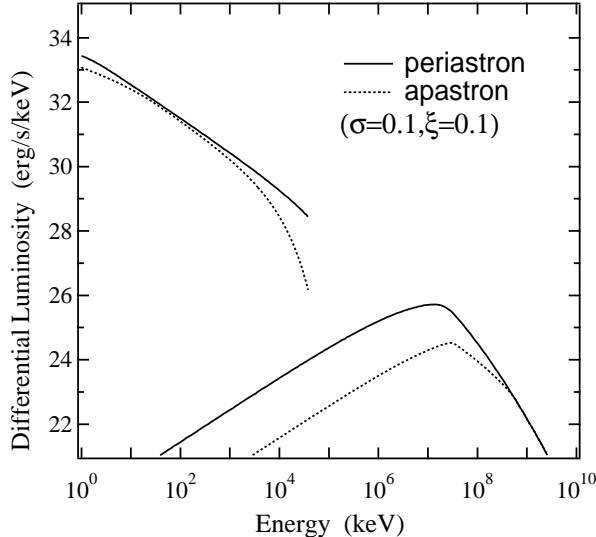


Fig. 7. Spectra of nebula emission at periastron (solid line) and apastron (dotted line). KeV–MeV photons are emitted by the synchrotron process, while GeV–TeV photons by the inverse Compton process. The model parameters used are the same as those in figure 5.

from equation (15) together with the Lorentz factor at the peak of the particle distribution. Hence, the minimum of the input Lorentz factor, which may lie near the peak of the particle distribution, can be estimated from the observed γ -ray energy at the peak. The peak height of the inverse Compton component decreases significantly with binary separation. We note that the density of target photons decreases in inverse proportion to the square of binary separation, while the number of relativistic electrons and positrons responsible for the peak in the whole nebula is determined by the flow time (or the escape time) and hence increases in proportion to the binary separation. In consequence, the inverse Compton scattering over the whole nebula becomes less frequent as the binary separation enlarges. The spectral curves, as seen from the periastron and apastron cases, converge and become independent of the binary separation near the highest end of γ -ray energies. We should note that the number of ultrarelativistic electrons and positrons responsible for these high energy γ -rays is determined by the synchrotron process and hence is inversely proportional to the energy density of the magnetic field whereas the inverse Compton scattering rate is proportional to the energy density of target photons. For constant ξ the ratio of magnetic energy density to photon energy density at the shock stays constant throughout the orbit, which results in the independence of spectral curves on the binary separation.

If the magnetic field at the shock is weak and the inverse Compton cooling dominates the synchrotron cooling, a larger number of relativistic electrons and positrons is required to produce such X-ray luminosity as shown in figure 7. Then, the GeV–TeV γ -ray luminosity is enhanced considerably compared to that in figure 7 (Kirk, Ball & Skjaeraasen 1999).

The adiabatic loss, even if included in calculations, yields only the slight change on the spectral curve in figure 7 and may not alter the essence of our results.

The target photons at the nebula are assumed here to be isotropic in computing the inverse Compton emission. In the case of photons from the Be star of a binary companion, the distribution of target photons may be closer to unidirectional rather than isotropic. Adopting the unidirectional distribution, Kirk, Ball & Skjaeraasen (1999) calculated the inverse Compton emission and show that the inverse Compton emission depends not only on the binary separation, but also on the binary orientation. We estimate from comparison of our computed spectra with their results that the effects of target photon distribution may produce a change of less than a factor of a few in the high energy γ -ray spectrum of inverse Compton emission. Hence, the γ -ray spectra of inverse Compton component shown in figure 7 is approximate. The effects of binary orientation should be included in the model especially when we conduct the closer comparison with the high energy γ -ray observations of PSR 1259-63/Be star system.

The compression ratio, used in equations (8), (10) and (11), is fixed to 3 throughout the paper although it depends on the Lorentz factor and magnetization parameter of the upstream flow (Kennel & Coroniti 1984; Kirk & Duffy 1999). The value of 3 is appropriate when the upstream flow is highly relativistic and the magnetization parameter is very small. The compression ratio is ~ 2.6 for $\gamma_w \sim 10^5$ and $\sigma \sim 0.1$ used in figure 7. This change in compression ratio almost does not alter the synchrotron component in figure 7 while it slightly modifies the inverse Compton component.

5. Comparison with Observations

The soft and hard X-rays observed from the PSR B1259-63/SS 2883 system have the following characteristics (Hirayama et al. 1999): (1) the X-ray spectra are represented by a power law function that extends from 1 to 200 keV; (2) the spectral index varies with orbital phase, from ~ 2 at periastron to ~ 1.6 at apastron; (3) the X-ray luminosity in the 1–10 keV band varies with orbital phase by about an order of magnitude, from $\sim 10^{34}$ ergs/s near periastron to $\sim 10^{33}$ ergs/s at apastron, while just at periastron the light curve displays a drop by a factor of two compared to that slightly before or after the periastron; (4) the pulsation is absent in the X-ray time series.

We plot the photon spectral gradient (index) calculated at 5 keV for various model parameters as a function of the binary separation in figure 8. The shock positions in figures 8b and 8c are taken to be 3 and 5 times farther away from the pulsar, respectively, compared to that in figure 8a. The magnetic field strengths at the shock are larger for larger σ and smaller a and ξ , while the target photon densities are larger for larger ξ and smaller a . We assume that the distributions of relativistic electrons and positrons injected at the shock are the same irrespective of the binary phase. We fix the minimum and maximum Lorentz factors for the input particle distribution to $\gamma_1 \sim 8 \times 10^4$ and $\gamma_2 \sim 3 \times 10^7$, respectively. The change of the

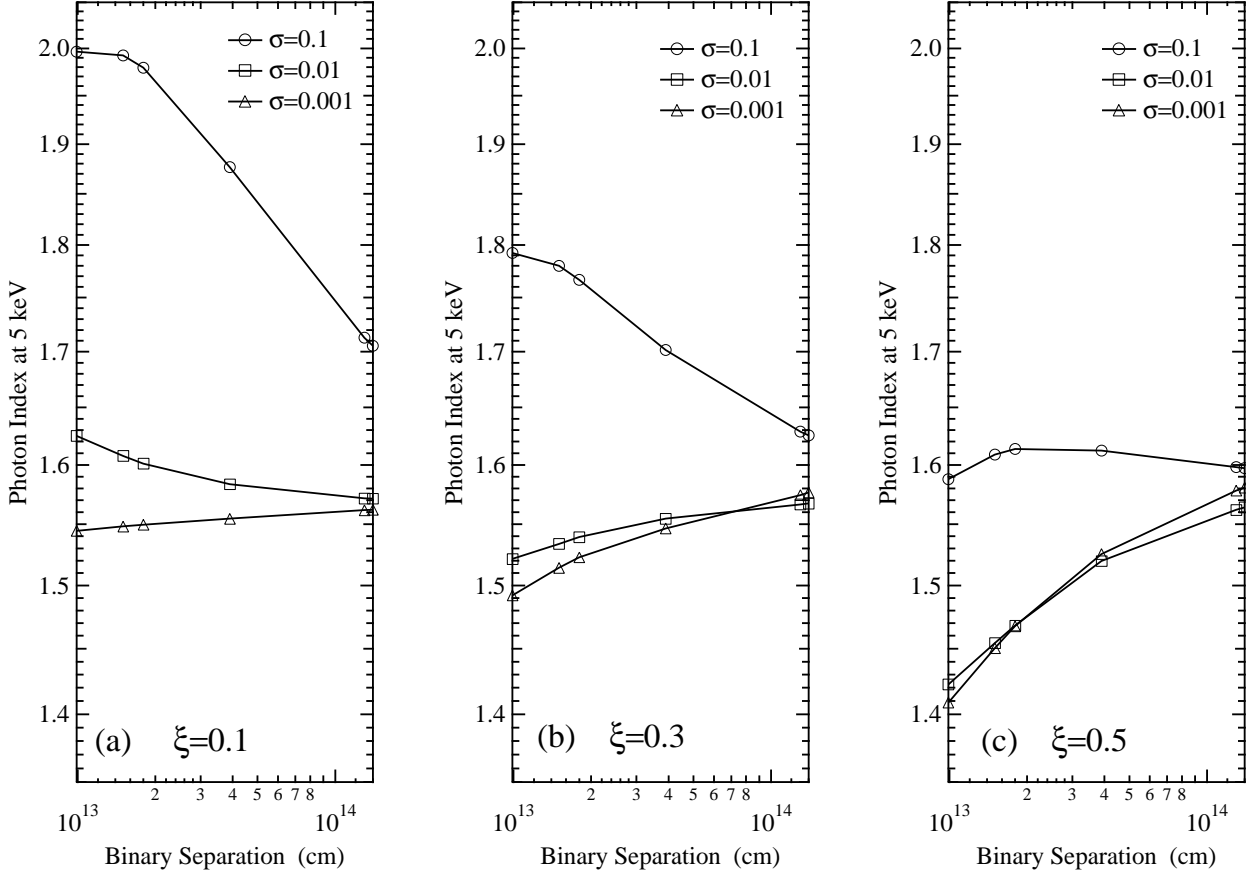


Fig. 8. Photon spectral indices calculated at 5 keV for various model parameters as a function of the binary separation. For larger σ and smaller ξ the synchrotron emission dominates over the inverse Compton scattering, leading to the spectral steepening. For smaller σ and larger ξ , on the other hand, the inverse Compton scattering dominates over the synchrotron emission, leading to the spectral flattening.

particle distribution in the nebula due to the radiative cooling is not significant at apastron. Hence, the photon spectral index at apastron reflects the original slope of the accelerated particle distribution. We adopt $p \sim 2.1$ determined from the photon index of ~ 1.6 observed at apastron. The observed photon index variation with orbital phase is approximately reproduced by the case with $\sigma \sim 0.1$ and $\xi \sim 0.1$ in figure 8a. Contrary to the results in figure 11 of Tavani & Arons (1997), we find that the efficient synchrotron cooling is responsible for the spectral steepening in the X-ray band around periastron. As clearly seen at periastron for $\sigma \sim 0.001$ in figures 8b and 8c, if the inverse Compton cooling dominates, the spectral slope rather flattens because of the Klein-Nishina effect. If the Klein-Nishina effect is fully taken into account, some results of Tavani & Arons (1997) may be altered.

If we choose $\xi \sim 0.1$ and $\sigma \sim 0.1$, the energy conversion parameter ε_a is determined to be ~ 0.1 from reproducing the relatively large X-ray luminosity observed at periastron. We

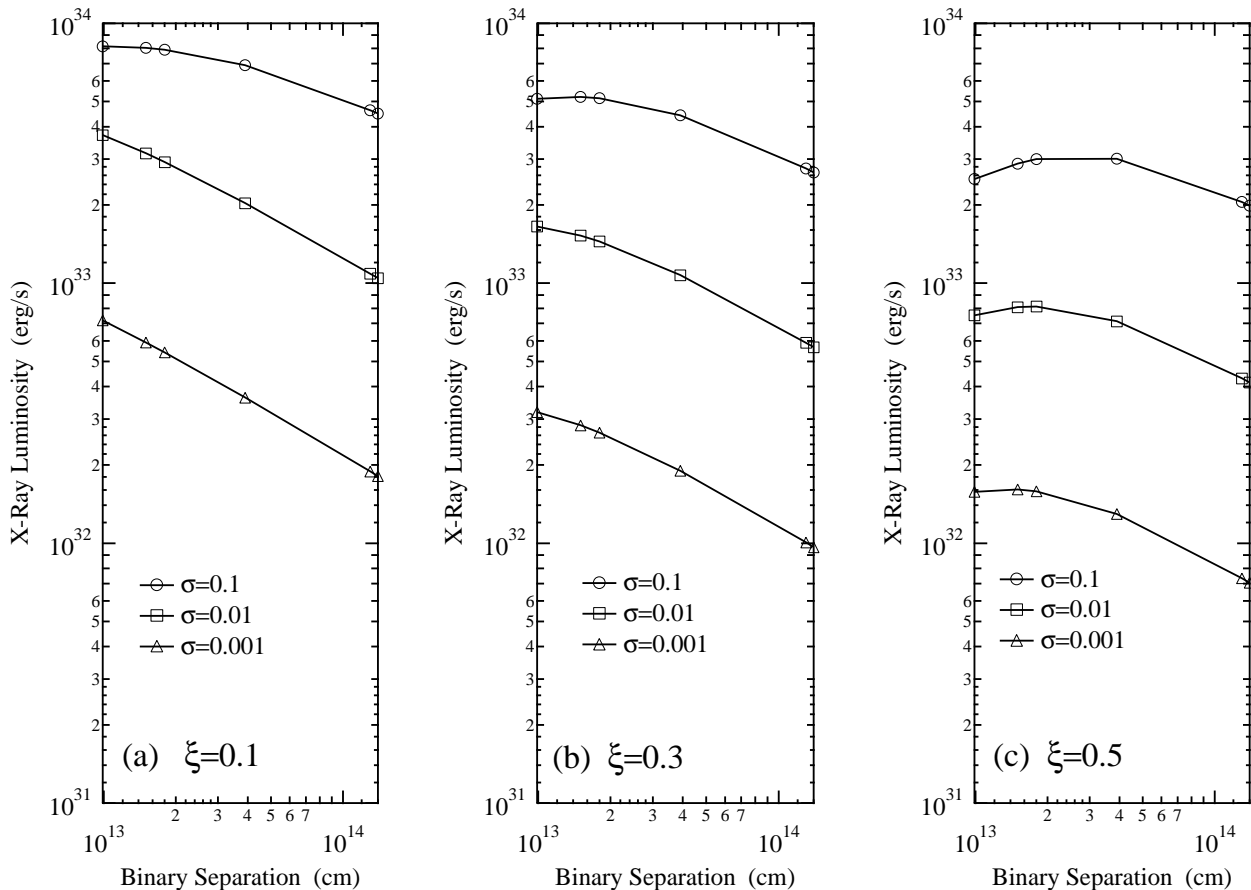


Fig. 9. Luminosity of X-rays in the 1–10keV band calculated for various model parameters as a function of the orbital separation. X-ray photons are emitted by the synchrotron process. The magnetic field strength in the nebula and hence the synchrotron emission rate decrease with decreasing σ .

depict the X-ray luminosity in the 1–10 keV band calculated for $\varepsilon_a \sim 0.1$ and various other model parameters as a function of the binary separation in figure 9. Note that, if the model parameters ξ and σ are taken to be constant throughout the binary orbit, the luminosity variation with orbital separation predicted by the model is too small to explain the observed variation amounting to an order of magnitude. We point out that this luminosity problem may be resolved if the magnetization parameter σ decreases with orbital separation and the shock position parameter ξ increases with orbital separation.

The magnetization parameter is likely to decrease with distance from the neutron star in the pulsar wind. Note that the small value of ~ 0.003 is reported for the Crab pulsar wind from the nebula analysis (Kennel & Coroniti 1984). In the Crab pulsar the distance of the shock, where the magnetization parameter is diagnosed, from the neutron star is ~ 0.1 pc, while in the PSR B1259-63 $\sim 10^{12} - 10^{13}$ cm. When combined with our result of the PSR B1259-63, the result of the Crab pulsar strengthens the conclusion that the magnetization parameter may

decrease with distance from the neutron star. The magnetization parameter and shock distance presented here can be used to study the property of a pulsar wind.

Our results shown in figure 7 are consistent with the COMPTEL and EGRET upper limits in the 1–1000 MeV range. Recently, the CANGAROO collaboration reports the new upper limit on the emission in the TeV range (Kawachi et al. 2002), which is well above our prediction and consistent with our results. Note, however, that the reproduction of a luminosity drop in X-rays, observed just at periastron, is beyond the scope of our simple model. We need to construct the detailed model that includes the binary orientation, the flow patterns of the Be star and pulsar winds, the misalignment of the pulsar orbital plane with the Be star outflow disk, the shielding of the emission region from the target photons for the inverse Compton scattering and the adiabatic loss in addition to the variation of model parameters σ and ξ with orbital separation.

6. Concluding Remarks

The PSR 1259-63/Be star system can provide important information on the pulsar wind. We can diagnose the property of the pulsar wind at various distances from the pulsar by applying the shock powered emission model to the X-ray fluxes and spectra observed at different orbital phases because the binary orbit is highly eccentric. We find that the magnetization parameter of the pulsar wind, the ratio of the Poynting flux to the kinetic energy flux, is ~ 0.1 at the distance of $\sim 10^{12}$ cm and may decrease with distance from the pulsar. Note that the magnetization parameter of the Crab pulsar wind is ~ 0.003 at the distance of ~ 0.1 pc. These two results, when combined, strengthen our conclusion that the magnetization parameter may decrease with distance from the neutron star. We need more X-ray data from various pulsar nebulae in order to determine the pulsar wind property as a function of distance from the pulsar and to understand the energy conversion from the Poynting flux to the kinetic energy flux in the pulsar wind.

The relativistic electrons and positrons of pulsar winds undergo inverse Compton scattering also upstream of the termination shock (Chernyakova & Illarionov 1999; Bogovalov & Aharonian 2000; Ball & Kirk 2000). Ball & Kirk (2000) show that γ -rays resulting from the inverse Compton scattering in the wind of PSR 1259-63 may be detectable by atmospheric Cerenkov detectors or by the programs INTEGRAL and GLAST if the size of the pulsar wind nebula is comparable to the binary separation. Then, we can diagnose directly the unshocked regions of pulsar winds previously thought to be invisible.

The PSR 1259-63/Be star system can also provide valuable information on the shock acceleration. We find that a fraction of ~ 0.1 of the pulsar energy is transformed into the relativistic electrons and positrons. We obtain the power law index of ~ 2 for the distribution of relativistic electrons and positrons injected at the shock. We should note that the maximum energy of accelerated electrons and positrons can be estimated from the break-off energy in

the photon spectrum. We expect this spectral break in the MeV–GeV range, which may be detectable by the future program GLAST. We may derive the minimum energy of relativistic electrons and positrons from the high energy γ -rays due to the inverse Compton emission. The observations of GeV–TeV γ -rays are also encouraged.

We thank M. Hirayama, F. Takahara and M. Hoshino for useful discussions and comments. We also thank the anonymous referee for valuable comments. This work was partly supported by a grant-in-aid of Ministry of Education, Culture, Sports, Science and Technology (12640302).

References

- Ball, L., & Kirk, J. G. 2000, *Astroparticle Phys.*, 12, 335
Blumenthal, G. R. 1970, *Rev. Mod. Phys.*, 42, 237
Bogovalov, S. V., & Aharonian, F. A. 2000, *MNRAS*, 313, 504
Chernyakova, M. A., & Illarionov, A. F. 1999, *MNRAS*, 304, 359
Cominsky, L., Roberts, M., & Johnston, S. 1994, *ApJ*, 427, 978
Greiner, J., Tavani, M., & Belloni, T. 1995, *ApJ*, 441, L43
Grove, J. E., Tavani, M., Purcell, W. R., Johnston, W. N., Kurfess, J. D., Strickman, M. S., & Arons, J. 1995, *ApJ*, 447, L43
Hirayama, M., Nagase, F., Tavani, M., Kaspi, V. M., Kawai, N., & Arons, J. 1996, *PASJ*, 48, 833
Hirayama, M., Cominsky, L. R., Kaspi, V. M., Nagase, F., Tavani, M., Kawai, N., & Grove, J. E. 1999, *ApJ*, 521, 718
Hoshino, M., Arons, J., Gallant, Y. A., & Langdon, A. B. 1992, *ApJ*, 390, 454
Hoshino, M., & Shimada, N. 2002, *ApJ*, 572, 880
Johnston, S., Lyne, A. G., Manchester, R. N., Kniffen, D. A., D’Amico, N., Lim, J., & Ashworth, M. 1992a, *MNRAS*, 255, 401
Johnston, S., Manchester, R. N., Lyne, A. G., Bailes, M., Kaspi, V. M., Guojun, Q., & D’Amico, N. 1992b, *ApJ*, 387, L37
Johnston, S., Manchester, R. N., Lyne, A. G., Nicastro, L., & Spyromilio, J. 1994, *MNRAS*, 268, 430
Jones, F. C. 1968, *Phys. Rev.*, 167, 1159
Kaspi, V. M., Tavani, M., Ngase, F., Hirayama, M., Hoshino, M., Aoki, T., Kawai, N., & Arons, J. 1995, *ApJ*, 453, 424
Kawachi, A. et al. 2003, to be submitted for publication
Kennel, C. F., & Coroniti, F. V. 1984, *ApJ*, 283, 694
Kirk, J. G., Ball, L., & Skjaeraasen, O. 1999, *Astroparticle Physics*, 10, 31
Kirk, J. G., & Duffy, P. 1999, *J. Phys. G*, 25, R163
Manchester, R. N., Johnston, S., Lyne, A. G., D’Amico, N., Bailes, M., & Nicastro, L. 1995, *ApJ*, 445, L137
Melatos, A., Johnston, S., & Melrose, D. B. 1995, *MNRAS*, 275, 381
Tavani, M., Arons, J., & Kaspi, V. M. 1994, *ApJ*, 433, L37

Tavani, M., Grove, J. E., Purcell, W., Hermsen, W., Kuiper, L., Kaaret, P., Ford, E., Wilson, R. B.,
Finger, M., Harmon, B. A., Zhang, S. N., Mattox, J., Thompson, D., & Arons, J. 1996, A&AS,
120, 221
Tavani, M., & Arons, J. 1997, ApJ, 477, 439
Taylor, J. H., & Cordes, J. M. 1993, ApJ, 411, 674